APPLIED PHYSICS

High coherence and low cross-talk in a tileable 3D integrated superconducting circuit architecture

Peter A. Spring[1]*†, Shuxiang Cao[1], Takahiro Tsunoda[1]‡, Giulio Campanaro[1], Simone Fasciati[1], James Wills[1], Mustafa Bakr[1], Vivek Chidambaram[1], Boris Shteynas[1], Lewis Carpenter[2]§, Paul Gow[2], James Gates[2], Brian Vlastakis[1]‖, Peter J. Leek[1]

We report high qubit coherence as well as low cross-talk and single-qubit gate errors in a superconducting circuit architecture that promises to be tileable to two-dimensional (2D) lattices of qubits. The architecture integrates an inductively shunted cavity enclosure into a design featuring nongalvanic out-of-plane control wiring and qubits and resonators fabricated on opposing sides of a substrate. The proof-of-principle device features four uncoupled transmon qubits and exhibits average energy relaxation times T_1 = 149(38) μs, pure echoed dephasing times $T_{\phi,e}$ = 189(34) μs, and single-qubit gate fidelities F = 99.982(4)% as measured by simultaneous randomized benchmarking. The 3D integrated nature of the control wiring means that qubits will remain addressable as the architecture is tiled to form larger qubit lattices. Band structure simulations are used to predict that the tiled enclosure will still provide a clean electromagnetic environment to enclosed qubits at arbitrary scale.

INTRODUCTION

Building two-dimensional (2D) lattices of hundreds or thousands of individually addressable, highly coherent qubits is an outstanding hardware challenge. Anticipated applications include demonstrations of logical gates using the surface code (*1*–*4*) and quantum simulations of 2D lattice Hamiltonians (*5*, *6*). Superconducting circuits are a promising platform for realizing such lattices (*6*–*8*); qubits are lithographically defined on 2D substrates, and tailored coupling circuitry can be included in the regions between qubits to realize a universal gate set. Two requirements for scaling such superconducting qubit lattices are (i) a method to route control wiring to the circuit such that all qubits remain addressable and measurable at progressively larger scales and (ii) a means of preventing low frequency spurious modes from emerging in the circuit as the dimensions increase (*9*). These modes can arise from sections of spurious planar transmission lines such as slotlines (*10*, *11*), or from 3D cavity enclosures that house the circuit (*11*). Solutions to these scaling challenges must not introduce substantial decoherence channels to qubits and, if fault tolerance is desired, must be compatible with gate fidelities beyond the thresholds of quantum error correction codes.

To overcome the wiring limitations of edge-connected circuits, 3D integrated control wiring is a practical solution. Various approaches to this have been demonstrated, for example, with spring-loaded pogo pins (*12*, *13*) and with galvanic bonding of the qubit substrate to a wiring/interposer substrate (*14*–*16*). To avoid spurious modes due to slotlines, divided ground planes can be inductively shunted with airbridges (*10*) or with superconducting through substrate vias (*15*, *17*, *18*). To avoid low-frequency cavity modes, one solution is to divide the quantum processor into subsystems, with each subsystem enclosed in a cavity with dimensions $\lesssim$1 cm (*19*–*22*). Alternatively, circuits can be enclosed in inductively shunted cavities that can scale arbitrarily in two dimensions with a cutoff frequency to cavity modes (*23*, *24*).

In this work, we present experimental results on a four-qubit proof-of-principle circuit incorporating this latter concept. The circuit architecture, based on that introduced in (*25*, *26*), features 3D integrated out-of-plane control wiring and qubits and readout resonators that are fabricated on opposing sides of a substrate. We incorporate a key new feature: inductively shunting the circuit enclosure with a pillar that passes through the substrate. This design is established to be compatible with transmon coherence times exceeding 100 μs, as well as low cross-talk and single-qubit gate errors. Simulations of band structure are used to predict that 2D qubit lattices can be formed by tiling a unit cell within the architecture, without the emergence of low-frequency cavity modes and with exponentially decaying cavity–mediated cross-talk between qubits.

RESULTS

Device architecture

Figure 1 shows optical images of the cavity enclosure and circuit. The enclosure base (Fig. 1A) features a single central "pillar", and the lid (Fig. 1B) contains a matching cylindrical recess that is filled with a ball of indium (Fig. 1C). The base and lid both contain four tapered through-holes that act as waveguides for qubit and resonator control signals. In Fig. 1D, the circuit substrate is shown placed inside the enclosure base. The 5000 ± 10 μm side lengths of the base recess and the 4975 ± 15 μm side lengths of the substrate set a maximum misalignment of the circuit to the enclosure of 25 μm. An aperture has been machined in the center of the substrate allowing the pillar to pass through. The four coaxial transmon (*27*) qubits are visible, arranged in a 2 × 2 lattice with 2-mm spacing.

Figure 2 shows a schematic of the out-of-plane wiring design, the inductive shunt design, and the circuit layout. Control signals are

[1]Clarendon Laboratory, Department of Physics, University of Oxford, Oxford OX1 3PU, UK. [2]Optoelectronics Research Centre, University of Southampton, Southampton SO17 1BJ, UK.
*Corresponding author. Email: peter.spring@riken.jp
†Present address: Center for Emergent Matter Science (CEMS), RIKEN, Wako, Saitama 351-0198, Japan.
‡Present address: Departments of Applied Physics and Physics, Yale University, New Haven, CT 06520, USA.
§Present address: SUNY Polytechnic Institute, 100 Seymour Road, Utica, NY 13502, USA.
‖Present address: Oxford Quantum Circuits, Thames Valley Science Park, Shinfield, Reading RG2 9LH, UK.

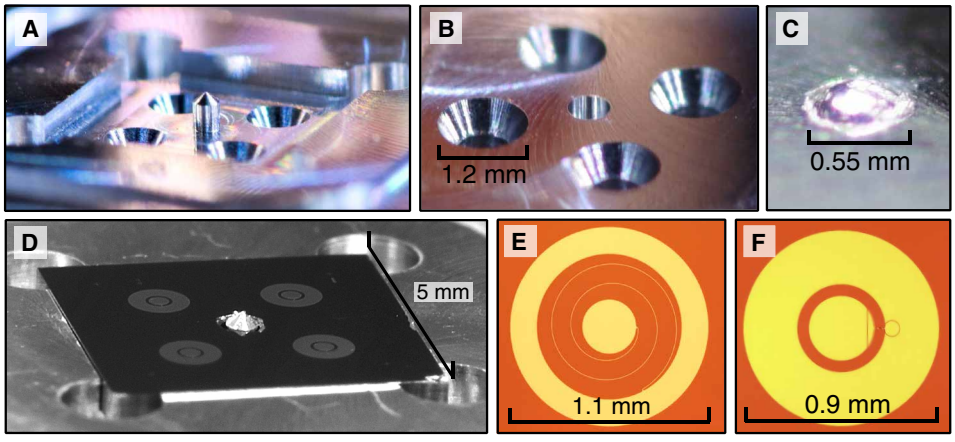

Fig. 1. Optical images of cavity enclosure and circuit. (**A**) Enclosure base with cavity, central pillar, and four tapered through-holes for out-of-plane wiring access. (**B**) Enclosure lid with a central cylindrical recess and identical through-holes for out-of-plane wiring. (**C**) Cylindrical recess in the lid filled with a ball of indium. (**D**) (Grayscale) Four-qubit circuit mounted inside the enclosure base. The four qubits are visible, arranged in a square lattice with 2-mm spacing. (**E**) A spiral resonator and (**F**) a transmon qubit with identical electrode dimensions to those in the device.

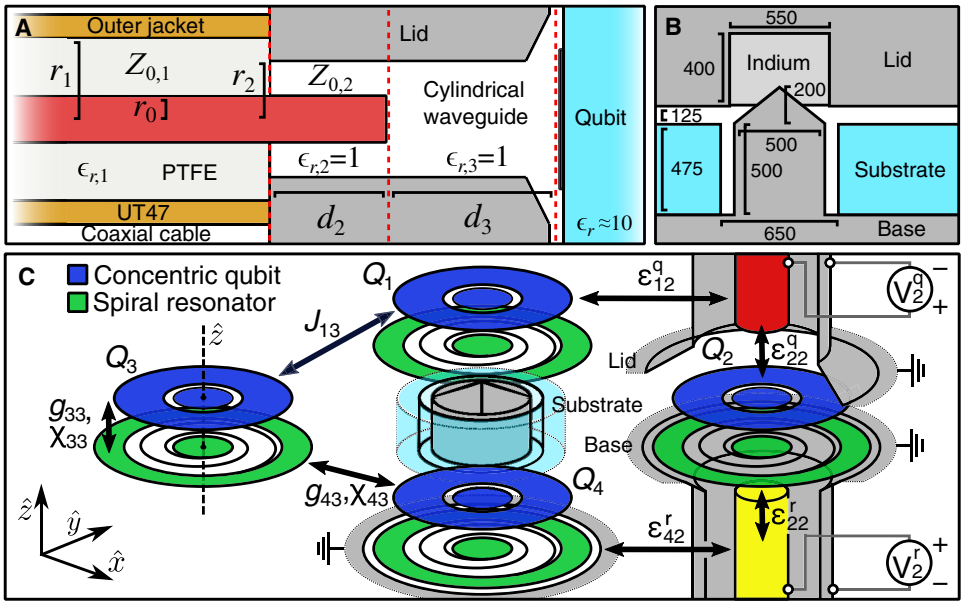

Fig. 2. Device schematics. (**A**) Cross section of the out-of-plane wiring design (not to scale), here shown addressing a qubit. PTFE, polytetrafluoroethylene. (**B**) Cross section of the bulk via inductive shunt design (to scale). The designed dimensions are shown in micrometers. (**C**) Circuit layout illustration (not to scale). The substrate and enclosure are partially shown, and the out-of-plane wiring is shown for Q_2. Examples of the coupling terms and drive voltages in the Hamiltonian in Eqs. 1 and 2 are shown.

routed to qubits and resonators by UT47-type coaxial cables with characteristic impedance $Z_{0,1} = 50 \pm 2.5$ ohms. As shown in Fig. 2A, the inner conductor of each cable, radius r_0, extends a distance d_2 into a through-hole in the circuit base/lid part, radius r_2, forming a coaxial waveguide with characteristic impedance $Z_{0,2}$. In this device, $r_0 = 145 \pm 2.5$ μm and $r_2 = 350 \pm 10$ μm (at room temperature), such that when ideally aligned $Z_{0,2} = 52.8 \pm 2.5$ ohms, a close match to the coaxial cable impedance $Z_{0,1}$. The polytetrafluoroethylene (PTFE) in the coaxial cable is separated from the circuit substrate by approximately 5 mm, reducing qubit/resonator electric field participation (*28*) in this lossy dielectric. The inner conductor of the coaxial cable terminates a distance d_3 from the qubit/resonator that it addresses. The coupling of control signals to qubits/resonators is dominantly mediated by an evanescent TM_{01} circular waveguide mode (*29*), with coupling strength $\varepsilon \propto \exp(-d_3/\delta_c)$, $\delta_c \approx r_2/2.4$. For $r_2 = 350$ μm, $\delta_c \approx 150$ μm. In this device, $d_3 \approx 0.9$ mm (0.4 mm) for each qubit (resonator) control line. Figure 2B shows a schematic cross section of the pillar in the enclosure base, passing through the aperture in the circuit substrate and into the recess in the enclosure lid. The galvanic connection is formed by the pointed tip of the pillar pressing into an indium ball in the lid recess, with the contact force being provided by titanium fasteners in the four corners of the enclosure part. The pillar acts as a "bulk via" that inductively shunts the two halves of the enclosure, without requiring side wall metallization of the substrate aperture or a galvanic connection between the substrate and enclosure. Figure 2C shows the circuit layout. The reverse side

of the substrate rests directly on the enclosure base and contains four lumped LC "spiral" resonators. Each resonator is coaxially aligned with and capacitively coupled to a qubit. The cavity enclosure provides the ground, and there are no ground planes on the substrate. The qubit (resonator) electrodes are electrically floating.

Basic characterization

An effective dispersive Hamiltonian for the low energy spectrum of the device is given by

$$\frac{\hat{H}}{\hbar} = \sum_{i=1}^{4} \omega_{q,i}\hat{a}_i^\dagger \hat{a}_i + \frac{\alpha_i}{2}\hat{a}_i^\dagger \hat{a}_i(\hat{a}_i^\dagger \hat{a}_i - 1) + \omega_{r,i}\hat{b}_i^\dagger \hat{b}_i + 2\chi_{ii}\hat{a}_i^\dagger \hat{a}_i \hat{b}_i^\dagger \hat{b}_i + \varepsilon_{ii}^q(\hat{a}_i - \hat{a}_i^\dagger)V_i^q + \varepsilon_{ii}^r(\hat{b}_i - \hat{b}_i^\dagger)V_i^r + \hat{H}_s/\hbar \quad (1)$$

Here, $\hat{a}_i^\dagger$ ($\hat{a}_i$) and $\hat{b}_i^\dagger$ ($\hat{b}_i$) are the creation (annihilation) operators for qubit i and resonator i, respectively; $\omega_{q,i}$ is the transition frequency of qubit i given zero photons in resonator i; α_i is the anharmonicity of qubit i; $\omega_{r,i}$ is the frequency of resonator i given qubit i is in its ground state; χ_{ii} is the dispersive shift between qubit i and resonator i; and ε_{ii}^q (ε_{ii}^r) describes the coupling of qubit (resonator) i to qubit (resonator) control line i, which is driven with a voltage V_i^q (V_i^r). These voltages are applied close to the cylindrical waveguide transition and at a fixed distance from the circuit (see Fig. 2C). $\hat{H}_s$ contains undesired cross-talk terms that are discussed in the cross-talk characterization section.

The quantities $\omega_{q,i}$, α_i, $\omega_{r,i}$, and χ_{ii} were determined using standard spectroscopic measurements and Ramsey measurements and are shown in Table 1. The relaxation times T_1 of the four qubits were simultaneously measured repeatedly over a period of 12 hours. The consecutive measured values and resulting histograms are shown in Fig. 3. The characteristic dephasing times T_2^* and $T_{2,e}$ were measured using standard Ramsey and Hahn echo pulse sequences (see the Supplementary Materials), performed on each qubit separately. Both characteristic dephasing times were measured repeatedly for approximately 2 hours per qubit. The coherence times are summarized in Table 2.

Cross-talk characterization

The device is a proof-of-principle demonstration of the circuit architecture with no intentional couplings except between qubit-resonator pairs; as such, we identify all other couplings as undesired cross-talk. The cross-talk terms that were considered are defined in the following effective Hamiltonian

$$\hat{H}_s/\hbar = \sum_{i,j(i\neq j)}^{4} J_{ij}\hat{a}_i^\dagger \hat{a}_j + 2\chi_{ij}\hat{a}_i^\dagger \hat{a}_i \hat{b}_j^\dagger \hat{b}_j + \varepsilon_{ij}^q(\hat{a}_i - \hat{a}_i^\dagger)V_j^q + \varepsilon_{ij}^r(\hat{b}_i - \hat{b}_i^\dagger)V_j^r \quad (2)$$

Here, J_{ij} is a parasitic transverse coupling between qubits i and j, satisfying $J_{ij} = J_{ji}$; χ_{ij} is a parasitic dispersive shift between qubit i and resonator j; and ε_{ij}^q (ε_{ij}^r) describes a parasitic coupling between qubit (resonator) i and qubit (resonator) control line j. Some examples of these different types of cross-talk are shown pictorially in Fig. 2C. The following expression was used to relate the dispersive shift χ_{ij} to a transverse coupling g_{ij} between transmon qubit i and resonator j (*27*)

$$\chi_{ij} \approx -\frac{(g_{ij})^2 E_{C,i}/\hbar}{\Delta_{ij}(\Delta_{ij} - E_{C,i}/\hbar)} \quad (3)$$

where $\Delta_{ij} = \omega_{q,i} - \omega_{r,j}$, and $E_{C,i}$ is the charging energy of qubit i.

The experimentally bounded maximum parasitic transverse couplings are summarized in Table 3, along with the predicted maximum values found by applying a simple impedance formula (*30*) to high-frequency structure simulator (HFSS)–driven terminal simulations (see the Supplementary Materials).

Qubit control line selectivity

The qubit control line selectivity φ_{ij}^q is here defined

$$\varphi_{ij}^q \stackrel{\text{def}}{=} \left(\frac{\varepsilon_{ij}^q}{\varepsilon_{jj}^q}\right)^2 \quad (4)$$

The selectivity was measured by driving qubit i at frequency $\omega_{q,i}$ from qubit control line j over a range of generator drive voltages $V_j^{q,\text{gen}}$ and fitting the induced Rabi oscillation rate Ω_i to the linear function $\Omega_i = k_{ij} V_j^{q,\text{gen}}$. From the measured linear response into the strong drive regime, it is inferred that the effective drive mediated by the J coupling between the qubits was negligible (see the Supplementary Materials). In this case, the selectivity takes the simple form $\varphi_{ij}^q = (k_{ij}/k_{jj})^2$. The measured qubit control line selectivities are shown in Fig. 4A, and the plots of Ω_i versus $V_j^{q,\text{gen}}$ that were used to determine φ_{21}^q are shown in fig. S4. The linear response in the strong drive regime also leads to a conservative experimental bound on the transverse coupling J_{ij}: $|J_{ij}| < [\min(\varphi_{ij}^q, \varphi_{j1}^q)]^{0.5} |\Delta_{ij}^q|$ (see the Supplementary Materials).

Resonator control line selectivity

The resonator control line selectivity φ_{ij}^r is here defined

Table 1. Basic device characterization. Summary of basic circuit parameters. The quantities ω_q, ω_r, α, χ, and g are as defined in the main text. The quantity $E_{J,i}/E_{C,i}$ is the ratio of the Josephson energy to the charging energy in qubit i; $\kappa_{\text{ext},i}$ is the external decay rate of resonator i; $Q_{\text{int},i}$ is the internal quality factor of resonator i; and $p_{e,i}$ is the residual excited state population in qubit i.

	$\omega_q/2\pi$ (GHz)	$\omega_r/2\pi$ (GHz)	$\alpha/2\pi$ (MHz)	E_J/E_C	$\chi/2\pi$ (kHz)	$g/2\pi$ (MHz)	$\kappa_{\text{ext}}/2\pi$ (kHz)	Q_{int} (10^3)	p_e (%)
Q_1/R_1	3.981	7.968	−199	69	−165	124	118	110	13
Q_2/R_2	4.045	8.083	−199	71	−167	126	73	75	18
Q_3/R_3	4.130	8.183	−198	74	−169	128	749	515	13
Q_4/R_4	4.192	8.289	−197	76	−164	128	241	160	10

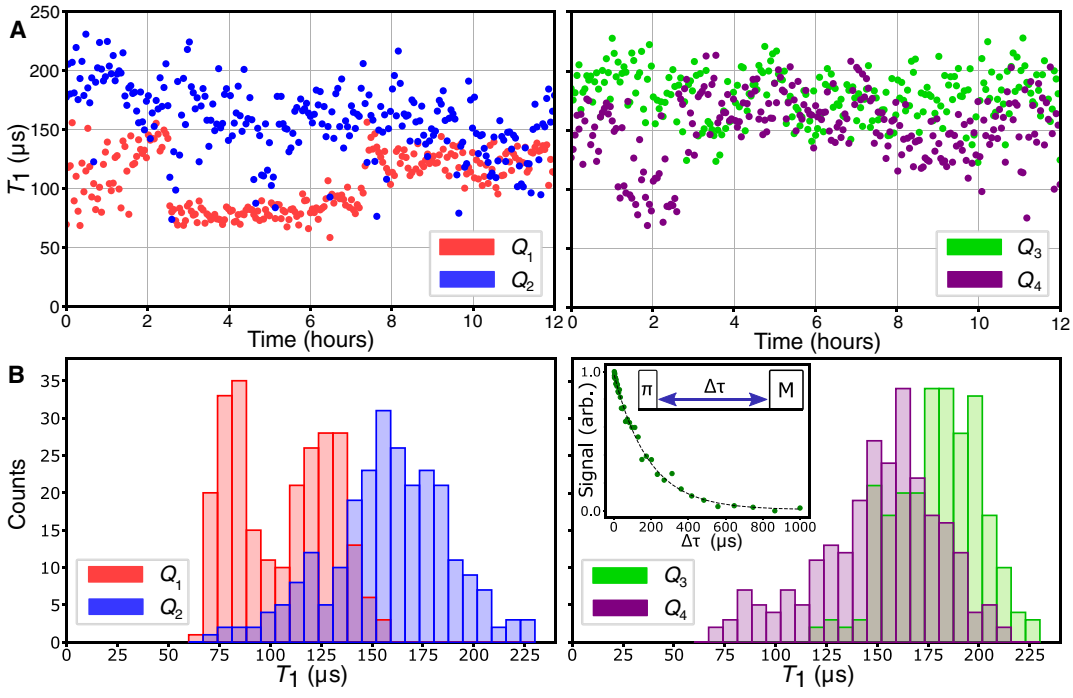

Fig. 3. Qubit relaxation characterization. (**A**) Two hundred fifty-one consecutive T_1 measurements over an approximately 12-hour period. (**B**) Resultant histograms of T_1. The inset shows an example T_1 time trace for Q_3, and the measurement pulse sequence. The four qubits were measured simultaneously; the data are shown across two graphs for legibility.

Table 2. Qubit coherence and gate errors. Summary of coherence results and error-per-physical gate (EPG) as found by separate (sep) and simultaneous (sim) randomized benchmarking. The pure echoed dephasing times are given by $1/T_{\phi,e} = 1/T_{2,e} - 1/(2T_1)$. The coherence limited EPG (EPG coh lim) was calculated as $(3 - \exp(-\tau_g/T_1) - 2\exp(-\tau_g/T_{2,e}))/6$ (*30*), where τ_g is the total period of each physical gate, here 24 ns.

	T_1(μs)	T_2^*(μs)	$T_{2,e}$(μs)	$T_{\phi,e}$(μs)	EPG sep (10^{-4})	EPG sim (10^{-4})	EPG coh lim (10^{-4})
Q_1	106(24)	95(5)	101(9)	193(52)	2.29(4)	1.64(4)	1.1(1)
Q_2	159(30)	104(9)	116(6)	183(25)	1.46(6)	2.15(8)	0.94(5)
Q_3	179(21)	89(12)	128(9)	199(25)	1.16(5)	1.31(5)	0.85(5)
Q_4	151(30)	99(8)	113(4)	181(24)	2.23(4)	2.16(4)	0.97(5)
Avg.	149(38)	97(10)	115(12)	189(34)	1.8(5)	1.8(4)	1.0(1)

$$\varphi_{ij}^r \triangleq \left(\frac{\varepsilon_{ij}^r}{\varepsilon_{jj}^r}\right)^2 \quad (5)$$

The selectivity was measured by continuously driving resonator i at a detuned frequency $\omega_{d,i} = \omega_{r,i} + \Delta_d$ from resonator control line j over a range of generator drive powers $P_j^{r,\mathrm{gen}}$. The induced AC Stark-shift $\omega_{\mathrm{AC},i}$ in qubit i was then fit to the linear function $\omega_{\mathrm{AC},i} = k'_{ij} P_j^{r,\mathrm{gen}}$. The selectivity is then given by $\varphi_{ij}^r = (\chi_{jj}/\chi_{ii})(k'_{ij}/k'_{jj})$ (see the Supplementary Materials). The measured resonator control line selectivities are shown in Fig. 4B, and the plots of $\omega_{\mathrm{AC},i}$ versus $P_j^{r,\mathrm{gen}}$ that were used to determine φ_{21}^r are shown in fig. S5.

Parasitic qubit-resonator coupling

To measure the parasitic dispersive shift χ_{ij} between qubit i and resonator j, resonator j was continuously driven at frequency $\omega_{r,j}$ from its own control line to populate it with a steady-state photon number $\bar{n}_j$ of at least $n_{\mathrm{crit},j}/10$, where $n_{\mathrm{crit},j} = (\Delta_{jj}/2g_{jj})^2$ is the critical photon number (*31*) of resonator j (see the Supplementary Materials). Ramsey experiments were then performed on qubit i ($i \neq j$) to measure the parasitic AC Stark-shift $\omega_{\mathrm{AC},i}$ as shown in Fig. 4C. No AC Stark-shift $\omega_{\mathrm{AC},i}$ was detected for any combination of qubit i and resonator j, with a frequency resolution of approximately 1 kHz, resulting in the approximate bound $\chi_{ij}/2\pi < 20$ Hz using the dispersive relation $\omega_{\mathrm{AC},i} = 2\chi_{ij}\bar{n}_j$ (*32*).

Single-qubit gate errors

Single-qubit randomized benchmarking (RB) (*33*, *34*) was performed on all four qubits both separately and simultaneously, using a combination of 24-ns duration (20-ns Blackman envelope with 4-ns buffer) physical I, $X_{\pi/2,\pi}$ gates with derivative removal gate (DRAG) pulse shaping (*35*), and virtual Z gates (*36*). Single-shot readout was performed for all the RB experiments (see Materials and Methods). Figure 5A shows the fitted RB curves for the simultaneous RB experiment. The RB protocol was run at 31 Clifford sequence lengths and for $k = 80$ different sequences of Clifford gates. Each of the 31×80 experiments was repeated 5000 times to build statistics. The resulting error-per-physical gates (EPGs) are presented in Table 2.

Table 3. Bounds on parasitic transverse couplings. Experimentally determined bounds on the magnitude of parasitic transverse couplings in the device, and the maximum predicted values between any qubit-qubit/qubit-resonator pair found using HFSS-driven terminal simulations and an impedance formula (*30*).

Cross-talk quantity	Experiment (kHz)	Simulation (kHz)
Qubit-qubit coupling $\lvert J \rvert/2\pi$	<250	10
Qubit-resonator coupling $\lvert g \rvert/2\pi$	<1500	50

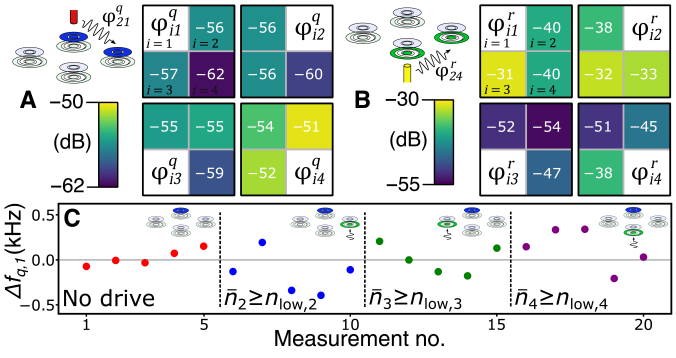

Fig. 4. Cross-talk characterization. (**A**) Experimentally measured qubit control line selectivity $\varphi^q_{ij} = (\varepsilon^q_{ij}/\varepsilon^q_{jj})^2$ from qubit *i* to qubit control line *j*, expressed in units of dB as $10\log_{10}(\varphi^q_{ij})$. (**B**) Experimentally measured resonator control line selectivity $\varphi^r_{ij} = (\varepsilon^r_{ij}/\varepsilon^r_{jj})^2$ from resonator *i* to resonator control line *j*, expressed in units of dB as $10\log_{10}(\varphi^r_{ij})$. (**C**) Frequency variation in Q_1 found from 20 repeated Ramsey experiments, with either no drive on any resonator or a continuous drive applied to R_2, R_3, or R_4 at frequency $\omega_{r,j}$ that populates it with a photon number $\bar{n}_j$ of at least $n_{\mathrm{low},j} \cong n_{\mathrm{crit},j}/10$.

Correlated RB (*37*) was performed using the simultaneous RB experiment data. Figure 5B shows a selection of the $2^4 - 1$ Pauli-Z correlators versus Clifford sequence length m. These were fit to standard RB curves $A\,\alpha_S^m + B$, where $S \subseteq B_4$, $S \neq \varnothing$, $B_4 = \{\{0\}, \{1\}, \{2\}, \{3\}\}$ as defined in (*37*). From the fitted depolarizing parameters α_S, the depolarizing fixed-weight parameters ϵ_S and the cross-talk metric $\tilde{\eta}$ were calculated (*37*). The ϵ_S parameters can be interpreted as the probability of a depolarizing error occurring in subspace S per Clifford gate, and $\tilde{\eta}$ is a scalar quantity that expresses the distance of the measured four-qubit error channel from the nearest product of single-qubit error channels (*37*). The calculated ϵ_S values are shown in Fig. 6, and we find $\tilde{\eta} \approx 1 \times 10^{-4}$ (see the Supplementary Materials).

Leakage RB (LRB) (*38*) was performed separately on Q_3, which had the highest readout fidelity (see Materials and Methods). The resultant LRB curve is shown in Fig. 5C, with a leakage-per-physical gate (LPG) of $3.49(7) \times 10^{-5}$; and an EPG of $2(1) \times 10^{-4}$ found using a four fit parameter model, and $2.33(7) \times 10^{-4}$ found using a more robust three fit parameter model that assumes EPG≫LPG (*38*).

Band structure simulations

Figure 7A shows an HFSS model of a unit cell that has dimensions exactly matching the ideal dimensions of the central 2 mm by 2 mm region of the device measured in this work. Figure 7B shows the simulated lowest-band dispersion of the infinite structure formed by tiling the plane with this unit cell, for both cases that the inductively shunting pillar and associated substrate aperture are included and are not included in the unit cell. In the case that the pillar is excluded, the band spans from 0 to 39.5 GHz, and undesired frequency collisions between qubits and this band are guaranteed. In contrast, when the pillar is present, the band has a cutoff frequency of $\omega_c/2\pi = 34.3$ GHz, with a bandgap below extending to 0 GHz. The simulated curvature around the cutoff frequency, defined $\omega_k = \omega_c + Ak^2$, where $k = \sqrt{k_x^2 + k_y^2}$, is $A/2\pi = 4.5$ GHz mm^2. A plasma metamaterial model (*39*, *40*) can be applied to the infinite structure (*23*, *24*) to predict a cutoff frequency at $\omega_c/2\pi = 35.9$ GHz and a band curvature of $A/2\pi = 8.8$ GHz mm^2, where these predictions neglect dissipation. This same metamaterial model can be used to predict that the spatial dependence for cavity-mediated transverse coupling between equal frequency qubits takes the form (*23*)

$$J_{\mathrm{cav},ij} = a\,K_0(d_{ij}/\delta_p) \tag{6}$$

Here, a is a spatially independent term, K_0 is the modified Bessel function of the second kind, d_{ij} is the spatial separation between qubits i and j, and $\delta_p = 1/\sqrt{\mu_0 \epsilon_0 \epsilon_r(\omega_c^2 - \omega_q^2)}$ is the plasma skin depth. Using the simulated value $\omega_c/2\pi = 34.3$ GHz results in a predicted plasma skin depth of $\delta_p \approx 0.7$ mm for the unit cell considered here, assuming $\omega_q \ll \omega_c$. The spatial dependence tends to $J_{\mathrm{cav},ij} \propto e^{-d_{ij}/\delta_p}/\sqrt{d_{ij}/\delta_p}$ for $d_{ij} \gg \delta_p$. This equates to $J_{\mathrm{cav},ij}$ decreasing by approximately 25 dB for each 2-mm increase in qubit separation. Cavity-mediated qubit(resonator)-control line couplings $\varepsilon^{q(r)}_{\mathrm{cav},ij}$ and qubit-resonator transverse couplings $g_{\mathrm{cav},ij}$ $(i \neq j)$ are likewise predicted to have the same spatial dependence. The band structure was mapped out using HFSS, with details on the simulation model as well as the analytical cutoff frequency, band curvature, and plasma skin depth predictions provided in the Supplementary Materials.

DISCUSSION

The architecture presented in this paper uses an inductively shunted cavity enclosure that tightly surrounds the circuit, combined with 3D integrated out-of-plane control wiring and "reverse-side" readout resonators. The results demonstrate that this design is compatible with transmon relaxation times T_1 at least in the range of 150 to 200 μs. The observed variation in T_1 is consistent with measured variation in transmon qubits on hour-long time scales and is suggestive of coupling to two-level system defects (*41*) as the dominant relaxation mechanism (*42*–*44*). The marked residual excited state population of the qubits suggests that quasiparticle-induced relaxation may also be significant (*45*, *46*), indicating a potential need for improved infrared filtering of signals to the device (*47*, *48*). We attribute the increase in coherence times compared to previous implementations of the architecture (*25*, *26*) mainly to the change in fabrication process (see Materials and Methods) and to the positioning of the out-of-plane control wiring, which ensured that qubits were not radiatively limited. The T_1 time purely due to radiation through all control and readout lines of the device was predicted to be ~5 ms using HFSS simulations (*49*, *50*) (see Supplementary Materials). Bringing in all the control lines by 100 μm in simulations, to model a significant misalignment of the out-of-plane wiring, reduces this radiation limited T_1 time to ~550 μs, implying that the measured qubit coherence times were robust to such a misalignment. The

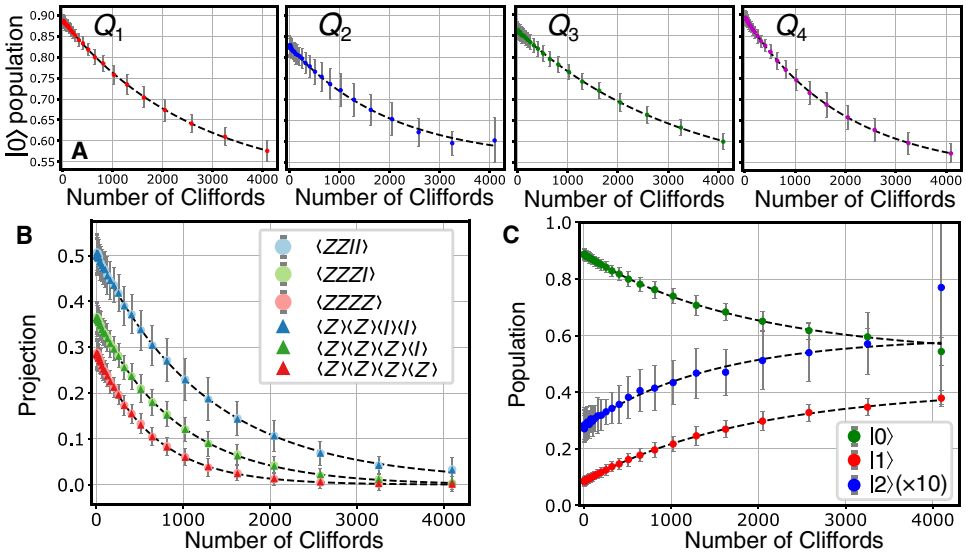

Fig. 5. Randomized benchmarking. (**A**) RB curves for simultaneous single-qubit RB on the four qubits. Points and error bars are the average and SD of the results for the $k = 80$ different Clifford sequences. (**B**) Pauli-Z correlators $\langle ZZII\rangle$, $\langle ZZZI\rangle$, and $\langle ZZZZ\rangle$ versus number of Clifford gates for the single-shot simultaneous RB data. The fitted dashed curves provide the depolarizing parameters α_{1100}, α_{1110}, and α_{1111}. The associated Pauli-Z products versus number of Clifford gates are also shown (triangles). The close similarity of the correlator and product curves is indicative of low cross-talk (*34*, *37*). (**C**) Leakage RB curve on Q_3. The final anomalous data point is excluded from the fit.

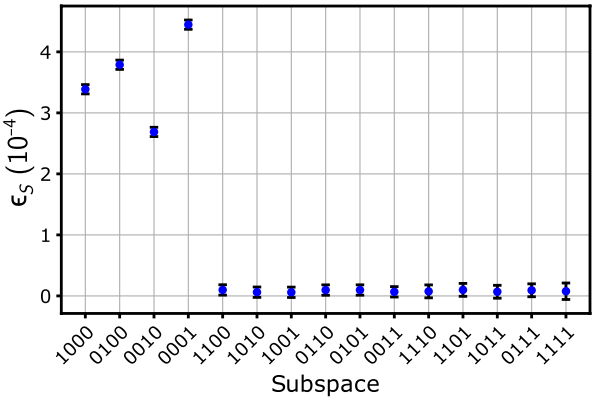

Fig. 6. Depolarizing fixed-weight parameters. The four-qubit system depolarizing fixed-weight parameters ϵ_S in each subspace S for $S \neq \varnothing$. The 15 subspaces are expressed as bitstrings, where if bit n (here indexed left to right) is 1, then qubit n is in that subspace.

architecture is also demonstrated to be compatible with pure echoed dephasing times $T_{\phi,e}$ of at least 180 μs. The average measured $T_{\phi,e}$ values bound the residual photon number and temperature of the four readout resonators to $\overline{n}_{\mathrm{th}} \leq 6.5 \times 10^{-3}$ and $T_r \leq 80$ mK (*51*). A possible topic for further work is to clarify the effect of mechanical vibrations in the out-of-plane wiring on qubit dephasing.

The results further establish that the architecture exhibits low cross-talk and can transmit short 20-ns control pulses that execute single-qubit gates of high fidelity $F \approx 99.98\%$. The average gate fidelity was the same within error for the separate and simultaneous RB, implying that cross-talk errors were inconsequential at the measured fidelity. The small value of the cross-talk metric $\tilde{\eta} \approx 1 \times 10^{-4}$ and the small values of ϵ_S for weight $|S| > 1$ show that depolarizing errors with weight $|S| > 1$ were highly suppressed. The average error per gate was approximately 50% coherence limited, and the leakage per gate as characterized on Q_3 was found to be less than 20% of the error per gate. These values might be improved in the future by more detailed pulse shaping and phase error correction (*37*).

The enclosure package could be reused by reshaping the indium ball in the lid recess to ensure a galvanic connection to the pillar on subsequent closure. The circuit was not bonded to the enclosure and could be removed and remounted. A limitation of the current enclosure design is that there was no contact force pressing the substrate to the enclosure. This could be improved by inserting spring-loaded pogo pins into the enclosure lid, which may enhance the circuit thermalization. In the current device, the single pillar in the enclosure is not expected to have contributed to the observed high coherence and low cross-talk results due to the small cavity size. However, these results are expected to be maintained on tiling to larger qubit arrays because of the inductive shunt array formed by the pillars, which causes the qubits to be exponentially insensitive to their nonlocal environment.

Experimentally realizing this tileability will rely on the ability to fabricate larger substrate aperture arrays and to manufacture larger arrays of 3D integrated out-of-plane wiring. Using the same methods as in the present work (see Materials and methods), we have successfully machined square aperture arrays with 2-mm pitch and featuring 725 apertures in 3-inch silicon substrates. Femtosecond laser machining and etching processes could also be explored to form these aperture arrays. Scaling the out-of-plane control wiring will require forming large arrays of 2-mm pitch coaxial waveguides. To minimize reflections and ensure uniform coupling of the control wiring to qubits and resonators, it would be desirable to have approximately 10-μm tolerances on the dimensions shown in Fig. 2A. We anticipate that this is a solvable engineering challenge.

Another important question is whether the introduction of qubit coupling circuitry between neighboring qubits will negate the

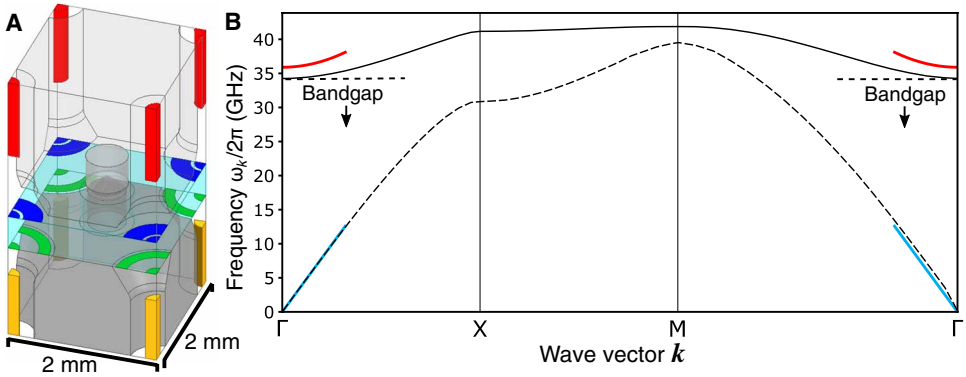

Fig. 7. Band structure simulation. (**A**) HFSS model of a unit cell featuring a single addressable and measurable qubit (4 × 1/4) and a single pillar that inductively shunts the enclosure. The unit cell has identical dimensions to the 2 mm by 2 mm central region of the device measured in this work. (**B**) Simulated lowest-band dispersion for the infinite enclosure formed by tiling the plane with the unit cell, with (solid) and without (dashed) the inductively shunting pillar and associated substrate aperture. The wave vector $\boldsymbol{k}$ traces between the symmetry points Γ : ($k_x = 0, k_y = 0$), X : ($k_x = \pi/a, k_y = 0$), M : ($k_x = \pi/a, k_y = \pi/a$). The colored curves show the predicted curvature around the Γ point with (red) and without (blue) the inductively shunting pillar and associated substrate aperture, using no free fit parameters (see the Supplementary Materials).

exponentially decaying cross-talk between qubits predicted here. We do not anticipate this to be the case. Idealized circuit models for 2D arrays of nearest neighbor coupling circuitry can be used to predict that, for qubit pitches that are significantly smaller than the excitation wavelength at qubit frequencies, this cross-talk channel will also be characterized by a cutoff frequency to spurious modes and exponentially decaying cross-talk with spatial separation.

A shortcoming of the presented device is that it exhibited small, variable external resonator decay rates $\kappa_{ext,i}$ and dispersive shifts χ_{ii} that were nonoptimal for qubit readout (*52*, *53*). The small and variable $\kappa_{ext,i}$ values may be attributed to slight movement of the control line inner conductors due to material contraction during cooling to cryogenic temperatures. The small χ_{ii} values were due to the large qubit-resonator detunings and the choice of qubit and resonator electrode dimensions. We anticipate that future devices can achieve improved readout parameters.

Takeaways

In this work, average transmon qubit coherence times of T_1 = 149(38) μs, $T_{\phi,e}$ = 189(34) μs, and simultaneous single-qubit gate fidelities of F = 99.982(4)% have been measured in a four-qubit demonstration of a 3D integrated superconducting circuit architecture. It has been shown that, before the inclusion of qubit coupling circuitry, residual cross-talk is highly suppressed. It is anticipated that a unit cell inside the device can be tiled to form larger devices that feature lattices of qubits. Band structure simulations predict that such devices will have a cutoff frequency to cavity modes that is well above qubit frequencies, in agreement with a metamaterial model that further predicts that cavity-mediated cross-talk between qubits in these lattices will decay exponentially with spatial separation. A potential near-term application for this architecture is the study of correlated errors generated by high energy radiation (*54*, *55*), where correlations could be probed in lattices of qubits with high coherence and exponentially suppressed cross-talk.

MATERIALS AND METHODS

The device enclosure was made from 6061 aluminum using computer numerical control (CNC) machining with ±10 μm tolerance on features. The out-of-plane wiring was made from silver-plated copper UT47 coaxial cable. The outer jackets and dielectrics were stripped back to expose the inner conductors (see fig. S2). The circuit was fabricated on a double-side polished high-resistivity intrinsic silicon wafer using a double-sided waferscale process. Following a hydrofluoric acid dip, aluminum was deposited onto both sides of the wafer by evaporation. The qubit and resonator electrodes were defined by a wet etching process, and the qubit Josephson junctions were formed using the Dolan Bridge double-angle shadow evaporation technique (*56*). After circuit fabrication, the wafer was diced into square dies with side lengths of 4975±15 μm using a Disco DAD3430 dicing saw, and a 650-μm diameter aperture was then CNC drilled in the center of selected dies using a Loxham Precision μ6 micromachining system. An approximately 0.5-μm-thick layer of S1805 photoresist was used as a protective layer during these CNC processes.

Qubit readout was performed using a standard heterodyne detection technique (*57*). It was possible to perform single-shot readout on all qubits by using 5-μs measurement pulses, with assignment fidelities: F = {97.8,97.7,98.5,98.4}%, where $F = 1 - p(e|g) - p(g|e)$ (*53*).

To extract the frequency of Ramsey fringes in Ramsey experiments, an interpolation method was applied to improve the frequency resolution found from the Fourier transform of the time traces (*58*). Details are provided in the Supplementary Materials.

Experiments were all carried out during a single cooldown inside an Oxford Instruments Triton 500 dilution refrigerator, with a base stage temperature of ~20 mK. A diagram of the dilution refrigerator setup is included in the Supplementary Materials.

SUPPLEMENTARY MATERIALS

Supplementary material for this article is available at https://science.org/doi/10.1126/sciadv.abl6698

REFERENCES AND NOTES

1. C. K. Andersen, A. Remm, S. Lazar, S. Krinner, N. Lacroix, G. J. Norris, M. Gabureac, C. Eichler, A. Wallraff, Repeated quantum error detection in a surface code. *Nat. Phys.* **16**, 875–880 (2020).
2. R. Barends, J. Kelly, A. Megrant, A. Veitia, D. Sank, E. Jeffrey, T. C. White, J. Mutus, A. G. Fowler, B. Campbell, Y. Chen, Z. Chen, B. Chiaro, A. Dunsworth, C. Neill, P. O'Malley,

P. Roushan, A. Vainsencher, J. Wenner, A. N. Korotkov, A. N. Cleland, J. M. Martinis, Superconducting quantum circuits at the surface code threshold for fault tolerance. *Nature* **508**, 500–503 (2014).
3. A. G. Fowler, M. Mariantoni, J. M. Martinis, A. N. Cleland, Surface codes: Towards practical large-scale quantum computation. *Phys. Rev. A* **86**, 032324 (2012).
4. S. B. Bravyi, A. Y. Kitaev, *Quantum Codes on a Lattice with Boundary* (1998); https://arxiv.org/abs/quant-ph/9811052.
5. Y. Yanay, J. Braumüller, S. Gustavsson, W. D. Oliver, C. Tahan, Two-dimensional hard-core Bose–Hubbard model with superconducting qubits. *npj Quantum Inf.* **6**, 58 (2020).
6. M. Gong, S. Wang, C. Zha, M. C. Chen, H. L. Huang, Y. Wu, Q. Zhu, Y. Zhao, S. Li, S. Guo, H. Qian, Y. Ye, F. Chen, C. Ying, J. Yu, D. Fan, D. Wu, H. Su, H. Deng, H. Rong, K. Zhang, S. Cao, J. Lin, Y. Xu, L. Sun, C. Guo, N. Li, F. Liang, V. M. Bastidas, K. Nemoto, W. J. Munro, Y. H. Huo, C. Y. Lu, C. Z. Peng, X. Zhu, J. W. Pan, Quantum walks on a programmable two-dimensional 62-qubit superconducting processor. *Science* **372**, 948–952 (2021).
7. F. Arute, K. Arya, R. Babbush, D. Bacon, J. C. Bardin, R. Barends, R. Biswas, S. Boixo, F. G. S. L. Brandao, D. A. Buell, B. Burkett, Y. Chen, Z. Chen, B. Chiaro, R. Collins, W. Courtney, A. Dunsworth, E. Farhi, B. Foxen, A. Fowler, C. Gidney, M. Giustina, R. Graff, K. Guerin, S. Habegger, M. P. Harrigan, M. J. Hartmann, A. Ho, M. Hoffmann, T. Huang, T. S. Humble, S. V. Isakov, E. Jeffrey, Z. Jiang, D. Kafri, K. Kechedzhi, J. Kelly, P. V. Klimov, S. Knysh, A. Korotkov, F. Kostritsa, D. Landhuis, M. Lindmark, E. Lucero, D. Lyakh, S. Mandrà, J. R. McClean, M. McEwen, A. Megrant, X. Mi, K. Michielsen, M. Mohseni, J. Mutus, O. Naaman, M. Neeley, C. Neill, M. Y. Niu, E. Ostby, A. Petukhov, J. C. Platt, C. Quintana, E. G. Rieffel, P. Roushan, N. C. Rubin, D. Sank, K. J. Satzinger, V. Smelyanskiy, K. J. Sung, M. D. Trevithick, A. Vainsencher, B. Villalonga, T. White, Z. J. Yao, P. Yeh, A. Zalcman, H. Neven, J. M. Martinis, Quantum supremacy using a programmable superconducting processor. *Nature* **574**, 505–510 (2019).
8. J. S. Otterbach, R. Manenti, N. Alidoust, A. Bestwick, M. Block, B. Bloom, S. Caldwell, N. Didier, E. Schuyler Fried, S. Hong, P. Karalekas, C. B. Osborn, A. Papageorge, E. C. Peterson, G. Prawiroatmodjo, N. Rubin, C. A. Ryan, D. Scarabelli, M. Scheer, E. A. Sete, P. Sivarajah, R. S. Smith, A. Staley, N. Tezak, W. J. Zeng, A. Hudson, B. R. Johnson, M. Reagor, M. P. da Silva, C. Rigetti, Unsupervised machine learning on a hybrid quantum computer. *Quantum Phys.* 10.48550/arXiv.1712.05771, (2017).
9. M. Kjaergaard, M. E. Schwartz, J. Braumüller, P. Krantz, J. I. J. Wang, S. Gustavsson, W. D. Oliver, Superconducting qubits: Current state of play. *Annu. Rev. Condens. Matter Phys.* **11**, 369–395 (2020).
10. Z. Chen, A. Megrant, J. Kelly, R. Barends, J. Bochmann, Y. Chen, B. Chiaro, A. Dunsworth, E. Jeffrey, J. Y. Mutus, P. J. J. O'Malley, C. Neill, P. Roushan, D. Sank, A. Vainsencher, J. Wenner, T. C. White, A. N. Cleland, J. M. Martinis, Fabrication and characterization of aluminum airbridges for superconducting microwave circuits. *Appl. Phys. Lett.* **104**, 052602 (2014).
11. S. Huang, B. Lienhard, G. Calusine, A. Vepsäläinen, J. Braumüller, D. K. Kim, A. J. Melville, B. M. Niedzielski, J. L. Yoder, B. Kannan, T. P. Orlando, S. Gustavsson, W. D. Oliver, Microwave package design for superconducting quantum processors. *PRX Quantum* **2**, 020306 (2021).
12. J. H. Béjanin, T. G. McConkey, J. R. Rinehart, C. T. Earnest, C. R. H. McRae, D. Shiri, J. D. Bateman, Y. Rohanizadegan, B. Penava, P. Breul, S. Royak, M. Zapatka, A. G. Fowler, M. Mariantoni, Three-dimensional wiring for extensible quantum computing: The quantum socket. *Phys. Rev. Appl.* **6**, 044010 (2016).
13. N. T. Bronn, V. P. Adiga, S. B. Olivadese, X. Wu, J. M. Chow, D. P. Pappas, High coherence plane breaking packaging for superconducting qubits. *Quantum Sci. Technol.* **3**, 024007 (2018).
14. B. Foxen, J. Y. Mutus, E. Lucero, R. Graff, A. Megrant, Y. Chen, C. Quintana, B. Burkett, J. Kelly, E. Jeffrey, Y. Yang, A. Yu, K. Arya, R. Barends, Z. Chen, B. Chiaro, A. Dunsworth, A. Fowler, C. Gidney, M. Giustina, T. Huang, P. Klimov, M. Neeley, C. Neill, P. Roushan, D. Sank, A. Vainsencher, J. Wenner, T. C. White, J. M. Martinis, Qubit compatible superconducting interconnects. *Quantum Sci. Technol.* **3**, 014005 (2017).
15. D. R. W. Yost, M. E. Schwartz, J. Mallek, D. Rosenberg, C. Stull, J. L. Yoder, G. Calusine, M. Cook, R. Das, A. L. Day, E. B. Golden, D. K. Kim, A. Melville, B. M. Niedzielski, W. Woods, A. J. Kerman, W. D. Oliver, Solid-state qubits integrated with superconducting through-silicon vias. *npj Quantum Inf.* **6**, 59 (2020).
16. D. Rosenberg, D. Kim, R. Das, D. Yost, S. Gustavsson, D. Hover, P. Krantz, A. Melville, L. Racz, G. O. Samach, S. J. Weber, F. Yan, J. L. Yoder, A. J. Kerman, W. D. Oliver, 3D integrated superconducting qubits. *npj Quantum Inf.* **3**, 42 (2017).
17. J. A. Alfaro-Barrantes, M. Mastrangeli, D. J. Thoen, S. Visser, J. Bueno, J. J. A. Baselmans, P. M. Sarro, Superconducting high-aspect ratio through-silicon vias with DC-sputtered Al for quantum 3D integration. *IEEE Electron Device Lett.* **41**, 1114–1117 (2020).
18. M. Vahidpour, W. O'Brien, J. T. Whyland, J. Angeles, J. Marshall, D. Scarabelli, G. Crossman, K. Yadav, Y. Mohan, C. Bui, V. Rawat, R. Renzas, N. Vodrahalli, A. Bestwick, C. Rigetti, Superconducting through-silicon vias for quantum integrated circuits. *J. Appl. Phys.* 10.48550/arXiv.1708.02226, (2017).
19. C. U. Lei, L. Krayzman, S. Ganjam, L. Frunzio, R. J. Schoelkopf, High coherence superconducting microwave cavities with indium bump bonding. *Appl. Phys. Lett.* **116**, 154002 (2020).
20. T. Brecht, Y. Chu, C. Axline, W. Pfaff, J. Z. Blumoff, K. Chou, L. Krayzman, L. Frunzio, R. J. Schoelkopf, Micromachined integrated quantum circuit containing a superconducting qubit. *Phys. Rev. Appl.* **7**, 044018 (2017).
21. T. Brecht, W. Pfaff, C. Wang, Y. Chu, L. Frunzio, M. H. Devoret, R. J. Schoelkopf, Multilayer microwave integrated quantum circuits for scalable quantum computing. *npj Quantum Inf.* **2**, 16002 (2016).
22. T. Brecht, M. Reagor, Y. Chu, W. Pfaff, C. Wang, L. Frunzio, M. H. Devoret, R. J. Schoelkopf, Demonstration of superconducting micromachined cavities. *Appl. Phys. Lett.* **107**, 192603 (2015).
23. P. A. Spring, T. Tsunoda, B. Vlastakis, P. J. Leek, Modeling enclosures for large-scale superconducting quantum circuits. *Phys. Rev. Appl.* **14**, 024061 (2020).
24. C. E. Murray, D. W. Abraham, Predicting substrate resonance mode frequency shifts using conductive, through-substrate vias. *Appl. Phys. Lett.* **108**, 084101 (2016).
25. J. Rahamim, T. Behrle, M. J. Peterer, A. Patterson, P. A. Spring, T. Tsunoda, R. Manenti, G. Tancredi, P. J. Leek, Double-sided coaxial circuit QED with out-of-plane wiring. *Appl. Phys. Lett.* **110**, 222602 (2017).
26. A. D. Patterson, J. Rahamim, T. Tsunoda, P. A. Spring, S. Jebari, K. Ratter, M. Mergenthaler, G. Tancredi, B. Vlastakis, M. Esposito, P. J. Leek, Calibration of a cross-resonance two-qubit gate between directly coupled transmons. *Phys. Rev. Appl.* **12**, 064013 (2019).
27. J. Koch, T. M. Yu, J. Gambetta, A. A. Houck, D. I. Schuster, J. Majer, A. Blais, M. H. Devoret, S. M. Girvin, R. J. Schoelkopf, Charge-insensitive qubit design derived from the Cooper pair box. *Phys. Rev. A* **76**, 042319 (2007).
28. C. Wang, C. Axline, Y. Y. Gao, T. Brecht, Y. Chu, L. Frunzio, M. H. Devoret, R. J. Schoelkopf, Surface participation and dielectric loss in superconducting qubits. *Appl. Phys. Lett.* **107**, 162601 (2015).
29. M. J. Reagor, *Superconducting Cavities for Circuit Quantum Electrodynamics* (Yale University, 2016), pp. 1–222.
30. F. Solgun, D. P. DiVincenzo, J. M. Gambetta, Simple impedance response formulas for the dispersive interaction rates in the effective Hamiltonians of low anharmonicity superconducting qubits. *IEEE Trans. Microw Theory Tech.* **67**, 928–948 (2019).
31. A. Blais, A. L. Grimsmo, A. Wallraff, Circuit quantum electrodynamics. *Rev. Mod. Phys.* **93**, 025005 (2021).
32. J. Gambetta, A. Blais, D. I. Schuster, A. Wallraff, L. Frunzio, J. Majer, M. H. Devoret, S. M. Girvin, R. J. Schoelkopf, Qubit-photon interactions in a cavity: Measurement-induced dephasing and number splitting. *Phys. Rev. A* **74**, 042318 (2006).
33. J. M. Chow, J. M. Gambetta, L. Tornberg, J. Koch, L. S. Bishop, A. A. Houck, B. R. Johnson, L. Frunzio, S. M. Girvin, R. J. Schoelkopf, Randomized benchmarking and process tomography for gate errors in a solid-state qubit. *Phys. Rev. Lett.* **102**, 090502 (2009).
34. J. M. Gambetta, A. D. Córcoles, S. T. Merkel, B. R. Johnson, J. A. Smolin, J. M. Chow, C. A. Ryan, C. Rigetti, S. Poletto, T. A. Ohki, M. B. Ketchen, M. Steffen, Characterization of addressability by simultaneous randomized benchmarking. *Phys. Rev. Lett.* **109**, 240504 (2012).
35. F. Motzoi, J. M. Gambetta, P. Rebentrost, F. K. Wilhelm, Simple pulses for elimination of leakage in weakly nonlinear qubits. *Phys. Rev. Lett.* **103**, 110501 (2009).
36. D. C. McKay, C. J. Wood, S. Sheldon, J. M. Chow, J. M. Gambetta, Efficient Z gates for quantum computing. *Phys. Rev. A* **96**, 022330 (2017).
37. D. C. McKay, A. W. Cross, C. J. Wood, J. M. Gambetta, Correlated randomized benchmarking. *Quantum Phys.* 10.48550/arXiv.2003.02354, (2020).
38. C. J. Wood, J. M. Gambetta, Quantification and characterization of leakage errors. *Phys. Rev. A* **97**, 032306 (2018).
39. J. B. Pendry, A. J. Holden, D. J. Robbins, W. J. Stewart, Low frequency plasmons in thin-wire structures. *J. Phys. Condens. Matter* **10**, 4785 (1998).
40. J. B. Pendry, A. J. Holden, W. J. Stewart, I. Youngs, Extremely low frequency plasmons in metallic mesostructures. *Phys. Rev. Lett.* **76**, 4773–4776 (1996).
41. C. Müller, J. H. Cole, J. Lisenfeld, Towards understanding two-level-systems in amorphous solids: Insights from quantum circuits. *Rep. Prog. Phys.* **82**, 124501 (2019).
42. J. J. Burnett, A. Bengtsson, M. Scigliuzzo, D. Niepce, M. Kudra, P. Delsing, J. Bylander, Decoherence benchmarking of superconducting qubits. *npj Quantum Inf.* **5**, 54 (2019).
43. P. V. Klimov, J. Kelly, Z. Chen, M. Neeley, A. Megrant, B. Burkett, R. Barends, K. Arya, B. Chiaro, Y. Chen, A. Dunsworth, A. Fowler, B. Foxen, C. Gidney, M. Giustina, R. Graff, T. Huang, E. Jeffrey, E. Lucero, J. Y. Mutus, O. Naaman, C. Neill, C. Quintana, P. Roushan, D. Sank, A. Vainsencher, J. Wenner, T. C. White, S. Boixo, R. Babbush, V. N. Smelyanskiy, H. Neven, J. M. Martinis, Fluctuations of energy-relaxation times in superconducting qubits. *Phys. Rev. Lett.* **121**, 090502 (2018).
44. C. Müller, J. Lisenfeld, A. Shnirman, S. Poletto, Interacting two-level defects as sources of fluctuating high-frequency noise in superconducting circuits. *Phys. Rev. B* **92**, 035442 (2015).
45. K. Serniak, M. Hays, G. de Lange, S. Diamond, S. Shankar, L. D. Burkhart, L. Frunzio, M. Houzet, M. H. Devoret, Hot nonequilibrium quasiparticles in transmon qubits. *Phys. Rev. Lett.* **121**, 157701 (2018).

46. G. Catelani, R. J. Schoelkopf, M. H. Devoret, L. I. Glazman, Relaxation and frequency shifts induced by quasiparticles in superconducting qubits. *Phys. Rev. B* **84**, 064517 (2011).
47. K. Serniak, S. Diamond, M. Hays, V. Fatemi, S. Shankar, L. Frunzio, R. J. Schoelkopf, M. H. Devoret, Direct dispersive monitoring of charge parity in offset-charge-sensitive transmons. *Phys. Rev. Appl.* **12**, 014052 (2019).
48. R. Barends, J. Wenner, M. Lenander, Y. Chen, R. C. Bialczak, J. Kelly, E. Lucero, P. O'Malley, M. Mariantoni, D. Sank, H. Wang, T. C. White, Y. Yin, J. Zhao, A. N. Cleland, J. M. Martinis, J. J. A. Baselmans, Minimizing quasiparticle generation from stray infrared light in superconducting quantum circuits. *Appl. Phys. Lett.* **99**, 113507 (2011).
49. S. E. Nigg, H. Paik, B. Vlastakis, G. Kirchmair, S. Shankar, L. Frunzio, M. H. Devoret, R. J. Schoelkopf, S. M. Girvin, Black-box superconducting circuit quantization. *Phys. Rev. Lett.* **108**, 240502 (2012).
50. A. A. Houck, J. A. Schreier, B. R. Johnson, J. M. Chow, J. Koch, J. M. Gambetta, D. I. Schuster, L. Frunzio, M. H. Devoret, S. M. Girvin, R. J. Schoelkopf, Controlling the spontaneous emission of a superconducting transmon qubit. *Phys. Rev. Lett.* **101**, 080502 (2008).
51. Z. Wang, S. Shankar, Z. K. Minev, P. Campagne-Ibarcq, A. Narla, M. H. Devoret, Cavity attenuators for superconducting qubits. *Phys. Rev. Appl.* **11**, 014031 (2019).
52. J. Heinsoo, C. K. Andersen, A. Remm, S. Krinner, T. Walter, Y. Salathé, S. Gasparinetti, J. C. Besse, A. Potočnik, A. Wallraff, C. Eichler, Rapid high-fidelity multiplexed readout of superconducting qubits. *Phys. Rev. Appl.* **10**, 034040 (2018).
53. T. Walter, P. Kurpiers, S. Gasparinetti, P. Magnard, A. Potočnik, Y. Salathé, M. Pechal, M. Mondal, M. Oppliger, C. Eichler, A. Wallraff, Rapid high-fidelity single-shot dispersive readout of superconducting qubits. *Phys. Rev. Appl.* **7**, 054020 (2017).
54. C. D. Wilen, S. Abdullah, N. A. Kurinsky, C. Stanford, L. Cardani, G. D'Imperio, C. Tomei, L. Faoro, L. B. Ioffe, C. H. Liu, A. Opremcak, B. G. Christensen, J. L. DuBois, R. McDermott, Correlated charge noise and relaxation errors in superconducting qubits. *Nature* **594**, 369–373 (2021).
55. J. M. Martinis, Saving superconducting quantum processors from decay and correlated errors generated by gamma and cosmic rays. *npj Quantum Inf.* **7**, 90 (2021).
56. G. J. Dolan, J. H. Dunsmuir, Very small ($\lesssim$ 20 nm) lithographic wires, dots, rings, and tunnel junctions. *Phys. B: Condens. Matter* **152**, 7–13 (1988).
57. A. Wallraff, D. I. Schuster, A. Blais, L. Frunzio, J. Majer, M. H. Devoret, S. M. Girvin, R. J. Schoelkopf, Approaching unit visibility for control of a superconducting qubit with dispersive readout. *Phys. Rev. Lett.* **95**, 060501 (2005).
58. M. Gasior, J. L. Gonzalez, Improving FFT frequency measurement resolution by parabolic and Gaussian spectrum interpolation. *AIP Conf. Proc.* **732**, 276 (2004).
59. M. Di Paolo Emilio, *Qiskit: An Open-source Framework for Quantum Computing* (EEWeb, 2021).
60. V. Tripathi, M. Khezri, A. N. Korotkov, Operation and intrinsic error budget of a two-qubit cross-resonance gate. *Phys. Rev. A* **100**, 012301 (2019).
61. M. Boissonneault, J. M. Gambetta, A. Blais, Improved superconducting qubit readout by qubit-induced nonlinearities. *Phys. Rev. Lett.* **105**, 100504 (2010).
62. J. Krupka, J. Breeze, A. Centeno, N. Alford, T. Claussen, L. Jensen, Measurements of permittivity, dielectric loss tangent, and resistivity of float-zone silicon at microwave frequencies. *IEEE Trans. Microw. Theory Tech.* **54**, 3995–4001 (2006).
63. P. A. Belov, S. A. Tretyakov, A. J. Viitanen, Dispersion and reflection properties of artificial media formed by regular lattices of ideally conducting wires. *J. Electromagn. Waves Appl.* **16**, 1153–1170 (2002).
64. A. Krynkin, P. McIver, Approximations to wave propagation through a lattice of Dirichlet scatterers. *Waves Random Complex Media* **19**, 347–365 (2009).

Acknowledgments: We would like to thank Loxham Precision for their support with milling parameters and tooling. **Funding:** This work has received funding from the U.K. Engineering and Physical Sciences Research Council under grant nos. EP/M013243/1, EP/N015118/1, EP/T001062/1, and EP/M013294/1 and from Oxford Quantum Circuits Limited. T.T. acknowledges support from the Masason Foundation and the Nakajima Foundation. S.F. acknowledges support from the Swiss Study Foundation and the Bakala Foundation. B.V. acknowledges support from an EU Marie Sklodowska-Curie fellowship. **Author contributions:** P.A.S. conceived the enclosure and circuit design, fabricated the circuit, performed the simulations and experiments, and analyzed the data. S.C. contributed to the FPGA firmware, the single-shot readout functionality, and to the device fabrication. T.T. contributed to the single-qubit gate pulse calibration and to the randomized benchmarking experiments. G.C. and S.F. contributed to the device fabrication. J.W. contributed to the device assembly and control electronics setup. M.B., V.C., and B.S. contributed to the cryogenic control setup. P.G., L.C., and J.G. diced the wafer and developed and carried out the CNC drilling of the circuit substrate. B.V. contributed to the enclosure design and helped supervise the device characterization. P.J.L. supervised the project. P.A.S. and P.J.L. wrote the manuscript. All authors discussed the results and provided feedback to the manuscript. **Competing interests:** P.A.S. and P.J.L. are inventors on patent applications related to this work (no. WO2020035672A1, P.A.S. & P.J.L.; no. WO2017021714A1, P.J.L.). P.A.S., P.J.L., S.F., G.C., V.C., and B.V. have received consultancy fees for related non-research activities from one of the funders of this work, Oxford Quantum Circuits Ltd. P.J.L. holds equity in Oxford Quantum Circuits Ltd. The other authors declare that they have no competing interests. **Data and materials availability:** All data needed to evaluate the conclusions in the paper are present in the paper and/or the Supplementary Materials. The data and analysis files are available at https://ora.ox.ac.uk/objects/uuid:53b3f9f3-16b3-4b1f-b81e-e8e6efd6e9b1.

Submitted 26 August 2021
Accepted 7 March 2022
Published 22 April 2022
10.1126/sciadv.abl6698

ScienceAdvances

High coherence and low cross-talk in a tileable 3D integrated superconducting circuit architecture

Peter A. SpringShuxiang CaoTakahiro TsunodaGiulio CampanaroSimone FasciatiJames WillsMustafa BakrVivek ChidambaramBoris ShteynasLewis CarpenterPaul GowJames GatesBrian VlastakisPeter J. Leek

Sci. Adv., 8 (16), eabl6698. • DOI: 10.1126/sciadv.abl6698